IEEE TRANSACTIONS ON DIELECTRICS AND ELECTRICAL INSULATION

This paper was submitted for review in June 2023. This work was partially supported by Project AIMS1, financed by the Malta Council for Science & Technology, for and on behalf of the Foundation for Science and Technology, through the FUSION: R&I Research Excellence Programme. *(Corresponding author: Hadi Naderiallaf).*

Hadi Naderiallaf is with the Power Electronics, Machine and Control Group (PEMC), The University of Nottingham, Nottingham, U.K. (e-mail: Hadi.Naderiallaf@nottingham.ac.uk).

Yatai Ji is with the Key Laboratory of More Electric Aircraft Technology of Zhejiang Province, University of Nottingham Ningbo, China, Ningbo, China. (e-mail: yatai.ji@nottingham.edu.cn).

Paolo Giangrande is with the Department of Engineering and Applied Sciences, University of Bergamo, Dalmine, Italy (e-mail: paolo.giangrande@unibg.it).

Michael Galea is with the Department of Industrial Electrical Power Conversion, University of Malta, Msida, Malta (e-mail: michael.d.galea@um.edu.mt).

IEEE TRANSACTIONS ON DIELECTRICS AND ELECTRICAL INSULATION

Temperature Impact on PDIV for Turn-to-Turn Insulation of Inverter-Fed Motors: from Ground Level to Cruising Altitude

H. Naderiallaf, Y. Ji, P. Giangrande and M. Galea

***Abstract*— Considering the turn-to-turn insulation as the most susceptible part to the failure of the electrical machine's insulation system in inverter-fed motors, this paper aims to elucidate the effect of temperature (*T*) on the streamer inception parameters (SIPs), including the Schumann constant (*K*), critical field line length (CFLL), air effective ionization coefficient (α_{eff}), and streamer inception field (E_{inc}). Particular attention is also given to extending the partial discharge inception (PDIV) modelling at cruising altitude (CA), equivalent to the air pressure of 200 mbar, as a function of *T* based on the Schumann streamer inception criterion (SCSIC), compared with the results obtained at 1000 mbar, i.e., ground level (GL). Furthermore, the ratios of SIPs and PDIV values at CA to those attained at GL are analysed as a function of *T*. The investigation findings serve as a prescription for electrical machine designers to enhance the insulating design of electrical machines used in More Electric Aircraft (MEA) applications.**

***Index Terms*— Electric machines, finite element analysis, insulation, partial discharges, reliability, temperature.**

NOMENCLATURE

B10	10^{th} percentile
CA	Cruising altitude
CFL	Critical field line
CFLL	Critical field line length
FEM	Finite element method
FL	Field line
FLL	Field line length
GL	Ground level
K	Schumann constant
MEA	More electric aircraft
p	Air pressure
PD	Partial discharge
PDIV	Partial discharge inception voltage
SCSIC	Schumann's streamer inception criterion
SIP	Streamer inception parameter
T	Temperature
TPs	Twisted pairs

I. INTRODUCTION

GLOBALLY recognized for their impact on decarbonization and better air quality, electric vehicles (EVs), hybrid electric vehicles (HEVs), MEA and all-electric aircraft (AEA) actively contribute to reducing CO_2 emissions, and global warming concerns [1]. Due to the improved torque/speed control, inverter-fed motors play a crucial role in transportation electrification and current trends to enable compact designs consist in adopting high DC bus voltages (e.g., 800 V) and increased *dV/dt* through wide bandgap devices like silicon carbide (SiC) and gallium nitride (GaN) semiconductors [2] and [3]. Furthermore, inverter-fed motors allow us to achieve considerable efficiency and enhanced performance, which are highly demanded in transportation applications [4].

Due to the reflections between the inverter and the machine winding, the winding turn-to-turn insulation of inverter-fed motors endures the highest electrical stress. First, voltage overshoots at the motor terminals are caused by the mismatch between the characteristic and surge impedances of the stator winding and the connecting cable [5]. Second, during the impulse flanks, most of the line voltage falls on the first turns near the machine terminals because of the high-frequency content of the steep-fronted PWM (Pulse Width Modulated) voltage waveforms during the rising and falling edges. Indeed, the voltage distributions along the winding are governed by the stray capacitances of the turn-to-ground and turn-to-phase in these circumstances because of the inductive/capacitive behaviour of the winding [6]. A real possibility exists for the electric field between turn-to-turn insulation to surpass the PD inception threshold. Particularly for type I insulation (i.e., organic insulating materials), insulation degradation may result if a single electron is available to start the PD process, leading to premature failure and shortening the lifetime to a few days if not hours [7]. Thus, the PD-free criterion must be taken into account while designing the insulation of inverter-fed machines so that the biggest peak voltage between turn-to-turn insulation should always be below the minimal peak of PDIV.

The gas number density or *p* reduction associated with CA in aerospace applications makes the PD inception more harmful than GL due to 1) a lower PDIV and 2) a significantly higher destructive potential of PD at CA [8], [9], [10]. Considering the latter, even Type II insulated wires (i.e., mixed organic-inorganic insulation known as corona-resistant wires), which can resist PD activity moderately in GL, cannot withstand PD inception at CA, giving a very short PD endurance period (i.e., shorter than one hour) [10]. The gas number density can become even lower with an increase in *T* at CA, implying intensified damage resulting from the PD activity. Furthermore, the PDIV reduction at CA and the high *T* values limit the maximum allowable DC bus voltage in

power converters, whose value is likely to be increased in future MEA applications for power density boosting purposes. Therefore, the insulation design of inverter-fed motors is more challenging for aerospace applications. The knowledge about the PD phenomenology at CA compared to GL considering the environmental conditions corresponding to the CA operational conditions such as T can support the insulation designers in the MEA industry.

Based on the hypothesis that streamer discharges are the prevailing reason for dielectric deterioration rather than Townsend discharges, this work endeavours to extend and improve the proposed simplified FEM model for PDIV in [11] based on SCSIC. In [11], PDIV was modelled at GL as a function of T based on B10 of measured PDIV reaching $K \approx 6$ at 1000 mbar. In this work, the PDIV model includes the behaviour of inverter-fed motors turn-to-turn insulation at CA (i.e., 200 mbar) vs T variations (i.e., 20°C-120°C) accounting for two different percentiles (i.e., mean and B10 of measured PDIV). In addition, the SIPs such as the K, CFLL, air effective ionization coefficient (α_{eff}), and streamer inception field (E_{inc}) are analysed at CA and GL against T change, presenting a comprehensive investigation. Furthermore, the SIPs and PDIV values ratios at CA to those acquired at GL as a function of T are examined to provide a better understanding of the PD phenomenology at CA (e.g., aerospace applications) against GL operations (e.g., automotive applications).

II. *K* Calculation

It is commonly accepted that when the number of electrons existing at the head of the avalanche reaches the earliest critical amount of N_c, the multiplication process becomes so rapid that fast-moving filamentary streamers incept to originate from the head of the avalanche [12]. In fact, the earliest critical avalanche would include approximately N_c electrons, over which the streamers' formation would occur [12]. An exponential function gives N_c as [13]:

$$N_c = exp(K) \#(1)$$

The dimensionless constant K determines the growth of streamers resulting from a single electron avalanche and is computed from (2) based on SCSIC [13], assuming that streamer discharges are the primary cause of the dielectric deterioration rather than Townsend discharges from GL to CA:

$$K = \int_0^{x_c} \alpha_{eff}(x) \cdot dx \ \#(2)$$

where x represents the distance from the avalanche's origin, incepting by a single primary electron. x_c is the length of the critical avalanche along the electric FL at which the streamer forms and α_{eff} is the air effective ionization coefficient given by:

$$\alpha_{eff} = \alpha - \eta \#(3)$$

where α and η are the gas ionization and attachment coefficients, respectively, changing as a function of gas type, electric field strength, gas number density or p, T, humidity, and pollution [12], [14].

During the experimental test campaign, the time between two successive PDIV tests is chosen long enough to allow for the decay or recombination of the deposited charges from the former measurement. As a result, the only way to initiate a discharge event is through air ionization [14]. Additionally, bipolar excitations featuring polarity reversal (e.g., AC) are preferred to voltage waveforms with a DC component (e.g., unipolar excitations) to avoid the impact of space charge accumulation on both field distribution in the air wedge and PDIV [15], [16], [17], [18].

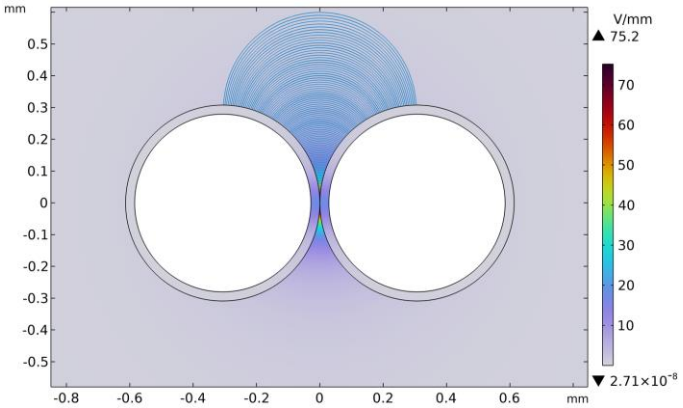

Fig. 1. The electrostatic simulation of non-uniform electric field distribution between two cylindrical insulated wires with a unit voltage using a 2D COMSOL Multiphysics®.

A. FLLs in the Air Wedge and Electric Field Intensity Simulation

Two-dimensional (2D) COMSOL Multiphysics® simulations based on the FEM model of the non-uniform electric field distribution in the air wedge between two cylindrical insulated wires are used for electrostatic calculations (Fig. 1). Considering the electric field distribution between the turn-to-turn insulation, the primary electrostatic simulation is conducted using a unit voltage (i.e., 1 V), while the simulation inputs are the dimensions of the wire cross-section (i.e., the bare wire diameter and insulation thickness) and the relative permittivity of the insulation. The output of the electrostatic simulation is enumerated as the reference database for the electric field distribution to calculate K. It consists of two data columns 1) FLLs only in the air wedge in mm, arranged from shortest to longest, and 2) the electric field intensity in V/m relevant to each FL, featuring a decreasing trend accordingly. While only the latter is promoted during the increasing voltage to find PDIV, which should be updated at each raising step, the former (i.e., FLLs) remains steady.

B. Deriving Effective Ionization Coefficient of Air as a Function of Electric Field Intensity

The ionization swarm parameters of dry air available in the LXCAT database, [19], [20], are loaded in the BOLSIG+

software to compute α/n and η/n as a function of the reduced electric field E/n. The ideal gas law, (4), delivers the gas number density, n, in m^{-3} as:

$$n = p \cdot V/k_{\mathrm{B}} \cdot T \#(4)$$

where p is in Pascals and V is the test volume in m^3 (e.g., the volume of vacuum chamber). T is expressed in Kelvin, and k_{B} is the Boltzmann constant, i.e., $1.380649\times10^{-23}\ J/K$.

The range limit of the reduced electric field, E/n, at which α/n and η/n should be calculated associated with the longest and shortest FLLs, respectively. In addition to the computation range limit, the moist air composition in percentage (%) and the gas T in Kelvin should be defined for the BOLSIG+ as inputs.

The moist air composition corresponding to the test condition can be approximated by (5), [21], since during the PDIV measurements, T and humidity are controlled and monitored constantly.

$$moist\ gas\ ratio\ (x) = dry\ gas\ ratio\ (x) \cdot (1 - M_{\mathrm{H_2O}}) \#(5)$$

where x is one of the air-forming gases such as Nitrogen (N_2), Oxygen (O_2), Argon (Ar), and carbon dioxide (CO_2). By volume, the dry air in Earth's atmosphere is about 78.08% N_2, 20.95% O_2, 0.93% Ar, and 0.04% CO_2 at 20°C [22]. Therefore, for example, $dry\ gas\ ratio\ (O_2)$ equals 20.95% in (5). Remarkably, diatomic oxygen, Argon, and carbon dioxide exhibit notable stability within the initial 80 km of altitude [23]. This suggests that the concentrations of these air-forming gases likely remain consistent up to our study's cruising altitude of 11.8 km (equivalent to 200 mbar). Consequently, it is assumed that the alteration in the dry gas mixing ratio only transpires via (5), with an increase in $M_{\mathrm{H_2O}}$ which is the water molar concentration in air calculated as [14]:

$$M_{\mathrm{H_2O}} = 0.622 \cdot \left(\frac{p_{\mathrm{H_2O}}}{p - p_{\mathrm{H_2O}}}\right) \#(6)$$

where 0.622 is the molar mass of water divided to that of air. $p_{\mathrm{H_2O}}$ is the water vapour pressure in Pascals, estimated by the empirical equation (7) as a function of air relative humidity, RH, and air T, t_{amb}, in °C [14]:

$$p_{\mathrm{H_2O}} = 611 \cdot RH \cdot 10^{7.5\left(\frac{t_{\mathrm{amb}}}{t_{\mathrm{amb}+237}}\right)} \#(7)$$

Considering (4) under a constant T, variations in p induce corresponding adjustments in n. This, in turn, triggers modifications in the reduced electric field (E/n) at a steady electric field strength. Due to the dependence of ionization (α), and attachment (η) coefficients on E/n, the BOLSIG+ software can calculate these coefficients as a function of E/n or E/p.

BOLSIG+ delivers α/n and η/n both in m^2 vs the reduced electric field, E/n, in Townsend. To match the unit of BOLSIG+ outputs to those of COMSOL simulations, while α_{eff}/n is calculated from (3), its unit is converted from m^2 to mm^{-1} as:

$$\alpha_{\mathrm{eff}}(mm^{-1}) = n \cdot \alpha_{\mathrm{eff}}/n \cdot 10^{-3} \#(8)$$

Moreover, it is required to convert the reduced electric field, E/n, from Townsend to the electric field in V/m using (9):

$$E(V/m) = n \cdot Townsend \cdot 10^{-21} \#(9)$$

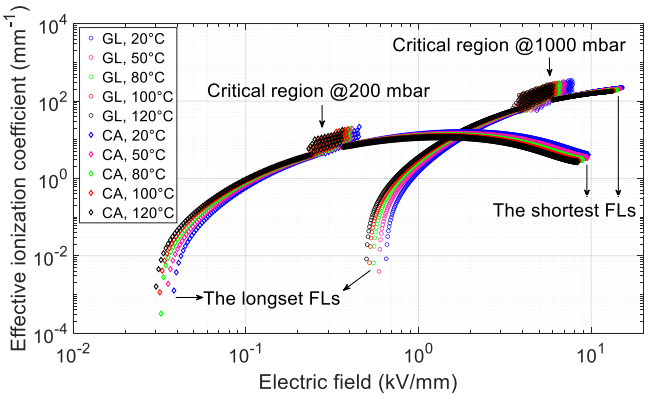

Fig. 2. T impact on α_{eff} from GL (1000 mbar) to CA (200 mbar) under PDIV corresponding to all the FLs ranging from the shortest FLL (E_{max}) to the longest FLL (E_{min}) derived by BOLSIG+.

Finally, Fig. 2 shows the final outputs of BOLSIG+, demonstrating the impact of T on α_{eff} from GL (1000 mbar) to CA (200 mbar), corresponding to all the FLs in the air wedge, ranging from the shortest FLL (E_{max}) to the longest FLL (E_{min}), considering (3) through (9). Fig. 2 illustrates a critical region or swollen area for each plot at which α_{eff} dispersion is promoted, increasing significantly once the electric field reaches that zone [21]. According to (4), both T rise and p drop lead to a reduction in gas number density. These two trends impact α_{eff} differently for the electric fields higher and lower than the critical region. For example, when the electric field is higher than that of the critical zone, increasing T and decreasing p result in α_{eff} decrement. However, the opposite holds when the electric field magnitude is lower than that of the critical zone. For the shortest FLLs, the effect of T rise on α_{eff} is more evident for CA than GL. For the longest FLLs, the influence of T increase on α_{eff} is tangible similarly for both CA and GL. Fig. 2 clarifies that the influence of p decrement from GL to CA is more remarkable than the effect of T increment, specifically within the investigated temperature range (20°C–120°C). Notably, while critical regions overlap for different temperatures at GL or CA, this region remains distinct for each. Moreover, Fig. 2 demonstrates that the critical region moves towards lower electric field intensities (i.e., longer FLLs) due to T enhancement and p reduction. However, the impact of the former is negligible compared with the latter from GL to CA. By comparing the critical region locations, the swollen area is closer to the shortest FLLs in the air wedge (i.e., the highest fields) at GL. Nevertheless, the swollen area is located almost in the middle of the plots (i.e., at lower electric fields than GL) when CA is considered. Thus, the CFLs obtained at CA would be longer than those attained at GL under PDIV.

C. Algorithm to Evaluate K under PDIV

An iterative algorithm [11] is implemented in the MATLAB environment to evaluate the experimental value of *K*. The algorithm relies on the measured turn-to-turn PDIV peak value as a function of *T* from GL (1000 mbar) to CA (200 mbar) using SCSIC. The iterative algorithm steps are detailed below.

1) Import the field distribution database: FLLs in mm vs electric field intensity across each FL in V/m computed by COMSOL for a unit voltage (i.e., 1 V), updating the latter using the measured peak value of PDIV (e.g., $PDIV_{mean}$ or $PDIV_{B10}$) as (10):

$$E(x,y) = PDIV \cdot E_{\text{database}}(x.y) \#(10)$$

2) Import the effective ionization database: α_{eff} in mm^{-1} vs electric field magnitude, E, in V/m calculated by BOLSIG+ shown in Fig. 2.

3) Evaluate the integral in (2), $\int_0^{x_c} \alpha_{\text{eff}}(x) \cdot dx$, for all air wedge FLs. Derive α_{eff} for each FL from Fig. 2 curves, accounting for the corresponding electric field intensity from (10) and the specific test conditions (*T* and GL or CA). The highest value from the integral across all FLs is denoted as *K*, and the associated FLL is identified as the CFLL [21].

III. Experimental Tests Campaign

Experimental data collection is necessary to evaluate the practical value of *K* for the turn-to-turn winding insulation. Therefore, the PDIV tests are carried out on TPs, which model the turn-to-turn insulation system. In the first subsection, the methodologies employed to measure bare wire diameter, insulation thickness, and relative permittivity are discussed. The test samples manufacturing is discussed in the second subsection, while the last two subsections address the PDIV test setup and the measurement conditions along with the test procedure respectively.

A. Bare Wire Diameter, Insulation Thickness, and Relative Permittivity Measurements

To perform the electrostatic computations shown in Fig. 1, the finite element model needs inputs such as the wire's cross-section geometry dimensions (i.e., bare copper diameter and insulation thickness) and the dielectric property which governs the electric field distribution (i.e., relative permittivity). A micrometre screw with an accuracy of 1 µm is used to measure the bare copper diameter and the insulation thickness. The difference in wire's diameter before and after stripping (thus, bare copper wire) divided by two gives the insulation thickness. The wires are stripped using a laser wire stripping apparatus to ensure that just the insulation and not any copper is removed. The required dimensions are evaluated using 20 wires, and the averaged values are then considered as the inputs for the electrostatic simulation. The mean measured bare copper diameter and mean insulation thickness are 556 µm and 28.5 µm, respectively.

The insulation's relative permittivity is calculated from the measured capacitance of a 10 cm painted wire with conductive paint at 50 Hz. One side of a wire is stripped to energize the copper using a sinusoidal voltage waveform. Conductive paint is used to paint 10 cm of the wire in the middle part to create the ground electrode [14]. The apparent capacitance is evaluated at 50 Hz in steps of 20 V from 20 to 100 V using a Megger Delta4000 at 20°C. It is worthwhile to mention that the relative permittivity does not change appreciably in the considered *T* range (i.e., 20°C-120°C). Thus, the measured permittivity at 20°C is valid for the electrostatic computations from 20°C to 120°C. Finally, the mean value of the measured capacitances over the voltage range is recorded, and the relative permittivity is calculated from (11), considering the average of the measured insulation capacitance over 20 painted wires as:

$$\varepsilon_{\text{r}} = \frac{C_{\text{w}}}{2\pi\varepsilon_0 l_{\text{p}}} \cdot \ln\left(\frac{D_{\text{w}}}{D_{\text{c}}}\right) \#(11)$$

where C_{w}, ε_0, l_{p}, D_{w} and D_{c} are the apparent capacitance of wire, free space permittivity (8.854×10^{-12} F/m), the length of the painted part, insulated wire diameter, and bare copper wire diameter, respectively. The mean calculated relative permittivity is equal to 4.31 F/m.

B. Test Samples for PDIV Measurements

The test samples are TPs made of grade II cylindrical magnet wires insulated with type I insulation (i.e., organic) and featuring 220°C thermal class (Fig. 3). The insulation overcoat and basecoat are polyamide-imide and THEIC-modified polyester-imide, respectively. In order to manufacture the TPs, the wires are twisted 12 times under a load tension of 7 N during the twisting process [24]. Five new (i.e., not electrically stressed) TPs are used to measure PDIV, generating the data set for each combination of *p* and *T*, e.g., GL and 20°C. PDIV is only assessed once for each test specimen as a fresh sample, ruling out the possibility of PDIV decreasing due to damages or deposited charges from the earlier tests [25].

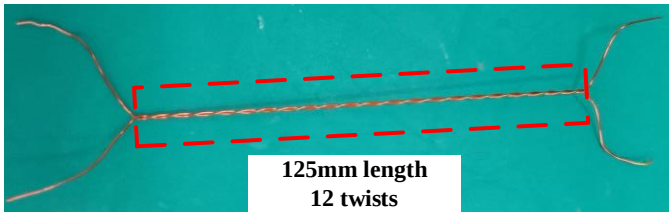

Fig. 3. A typical test specimen

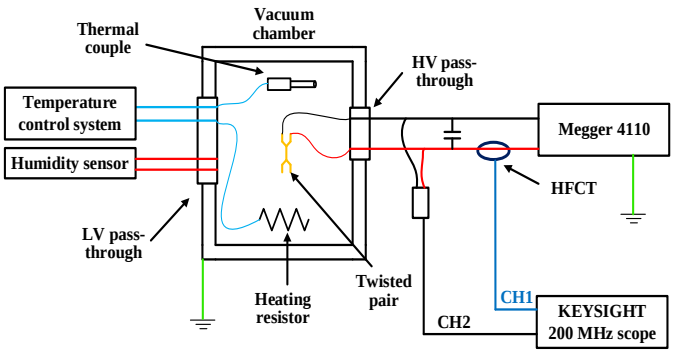

Fig. 4. Schematic diagram of the PDIV test setup and connections layout.

C. PDIV Test Setup

As allowed by IEC 60034-18-41 [26], the PDIV measurements are performed using 50 Hz sinusoidal voltage waveform excitations to qualify the turn-to-turn insulation of inverter-fed motors. When measuring PDIV at AC 50 Hz, the results can be slightly lower than those obtained using waveforms from 2-level inverters or surge generators [3], [27]. Therefore, to get conservative PDIV values, the tests are performed using AC 50 Hz excitations. A vacuum chamber with a test volume of 0.064 m^3 and the possibility of exact control of *T*, *p*, and humidity accommodates a group of five samples, which are energized and tested separately. Inside the test chamber, a humidity sensor (MIAO XIN TH10S-B-H) measures the humidity, while an electric heating element controlled by the industrial temperature controller regulates the *T*. The low voltage (LV) pass-through of the chamber allows the wiring of both the humidity sensor and temperature controller. The Megger 4110 generates the AC 50 Hz excitation voltage, which is measured by a high voltage (HV) differential probe (PICO® TA044) featuring 70 MHz bandwidth, 1000:1 voltage attenuation ratio, and 10 MΩ impedance. The excitation voltage is then monitored through a Keysight® DSOX2024A oscilloscope. A conventional indirect circuit, schematically shown in Fig. 4, is adapted to acquire the PD signals. A PD-free 4.7 nF coupling capacitor is connected in parallel with the test specimen to improve the signal-to-noise ratio and enhance the measurement sensitivity. The PD sensor is a ferrite-core high-frequency current transformer (HFCT) with a bandwidth of 0.3–100 MHz made by Kanggaote (KGT) and connected directly to the oscilloscope.

D. Measurement Conditions and Test Method

The PDIV tests are conducted at two *p* values: 1000 and 200 mbar, corresponding to GL and CA, respectively, at five different *T* values: 20, 50, 80, 100, and 120°C. Throughout the testing, the humidity is continuously measured and set at the appropriate absolute humidity (AH) level of 3.78 g/m^3, which corresponds to the relative humidity (RH) of 22% at 20°C, and 1000 mbar [8].

For each test specimen, the PDIV is measured by increasing the excitation voltage peak in steps of 10 V, and a waiting time of 30 s (for GL) and 240 s (for CA) is applied between two consecutive steps. The waiting time is longer at CA (200 mbar) since a PD is initiated once the two conditions are fulfilled simultaneously: (1) the electric field in the air wedge between the two wires becomes higher than the inception field, and (2) a free electron gets available to start the avalanche. Free electrons are made available through the gas molecules photoionizing [6], and such a phenomenon is mitigated at reduced *p*, like in the case of CA conditions, due to the reduced gas number density.

The measured PDIV is reported as the mean peak value of PDIV and as B10 of the 2-parameter Weibull distribution. Additionally, using the shape/slope parameter of the Weibull distribution (i.e., β), the measurement dispersion level is examined quantitatively.

IV. Results and Discussions

SIPs and PDIV prediction are conducted using more than one percentile of PDIV, e.g., the PDIV mean measured peak values (i.e., $PDIV_{mean}$) and the B10 of the PDIV peak (i.e., $PDIV_{B10}$). This choice allows us to evaluate the trends of SIP vs *T* by relying on two PDIV percentiles to verify which *K* value (i.e., based on $PDIV_{mean}$ or $PDIV_{B10}$) delivers the best PDIV forecast. Additionally, due to the PD's stochastic nature, the availability of two PDIV percentiles also enables to clarify when the PDIV dispersion level is lower (i.e., β is higher), referring to different percentiles of the PDIV can deliver comparable results for SIPs.

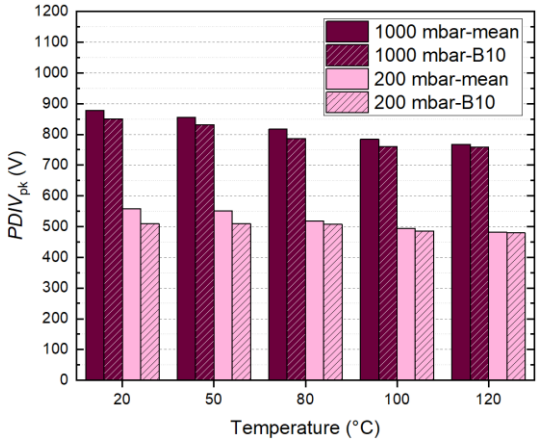

Fig 5. Measured mean and B10 of PDIV peak at 1000 and 200 mbar as a function of *T*.

A. PDIV and Its Dispersion

Fig. 5 shows the PDIV drop vs *T* rise, which can be ascribed to a lower gas density, thus a longer mean free path at a higher *T*. Indeed, when the discharge path is more extended, electrons can attain more kinetic energy along a FL, reaching the critical number of electrons in the head of the avalanche at a lower voltage level. It is worthwhile to recall that the increase of enamel permittivity in the *T* range under investigation can be negligible since the glass transition *T* (i.e., T_g) of Polyamide-imide is higher than 240°C (e.g., 275°C for

Solvay Torlon) [28]. In addition, the swarming parameters are not significantly affected by T in the 25°C-200°C range [29].

The PDIV dependency on T from GL to CA is examined by fitting the measured values via linear regression as:

$$PDIV_{\mathrm{pk}}(T) = -A \cdot T + B, \qquad T \in [20℃, 120℃] \#(12)$$

where A and B are the slope and width from the origin of the linear regression, respectively, listed in Table I, also indicating the coefficient of determinations, R^2, corresponding to each combination of pressure and percentile values.

TABLE I
LINEAR REGRESSION PARAMETERS AND GOODNESS COEFFICIENT

pressure & percentile	1000 mbar-mean	1000 mbar-B10	200 mbar-mean	200 mbar-B10
A	1.15	1.03	0.83	0.32
B	905.37	873.83	581.84	522.1
R^2	0.99	0.96	0.96	0.76

From Table I, the PDIV dependency on T at GL is higher since $A_{200\,\mathrm{mbar}} < A_{1000\,\mathrm{mbar}}$, for both mean and B10 of PDIV. The lower PDIV variation at CA can be ascribed to its lower gas density where the chance of air molecules incident resulting from T rise is lower than GL. Furthermore, a lower percentile of the distribution (e.g., B10) shows a lower variation of PDIV vs T as $A_{\mathrm{B10}} < A_{\mathrm{mean}}$. In addition, a linear regression of PDIV against T gives a more accurate fitting to the measured values if it refers to mean value rather than B10 of PDIV since $R^2{}_{\mathrm{B10}} < R^2{}_{\mathrm{mean}}$ especially for CA.

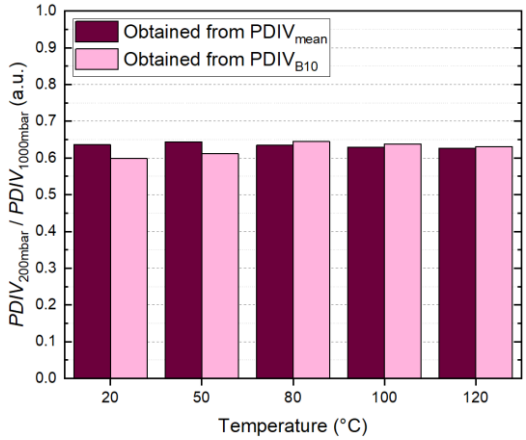

Fig 6. The ratio of measured mean and B10 of PDIV at CA to GL as a function of T.

Fig. 6 represents that the ratio of measured PDIV at CA to GL remains almost stable vs T around 0.63 and 0.62 based on $\mathrm{PDIV}_{\mathrm{mean}}$ and $\mathrm{PDIV}_{\mathrm{B10}}$, respectively. This finding is helpful to estimate PDIV vs T at CA if the PDIV trend against T at GL and the PDIV value at CA only for a particular T are known. Indeed, the finding would enable time-saving in test campaigns and lower equipment requirements.

Fig. 7 displays the measured PDIV dispersion level vs T, relying on the shape/slope parameter of the 2-parameter Weibull distribution (i.e., β). It shows that the dispersion level of PDIV decreases (i.e., β increases) at CA with respect to T rise. β of PDIV remains almost stable at GL from 20°C to 100°C, while it reaches a maximum value at 120°C for both GL and CA. Since the enamel surface work function reduces at a higher T, the electron emission rate can increase based on the Schottky-Richardson emission mechanism [30], leading to a higher β. However, this effect is more evident at CA due to a lower gas density, thus a lower probability for the attachment of the released electrons compared with the denser air at GL. Additionally, while at higher T values in the 80°C-120°C range, $\beta_{200\,\mathrm{mbar}} > \beta_{1000\,\mathrm{mbar}}$ (about 2.76 times at 120°C), the opposite holds in the 20°C-50°C range where $\beta_{200\,\mathrm{mbar}} < \beta_{1000\,\mathrm{mbar}}$ (about 2.75 and 2.79 times, respectively, at 20°C and 50°C).

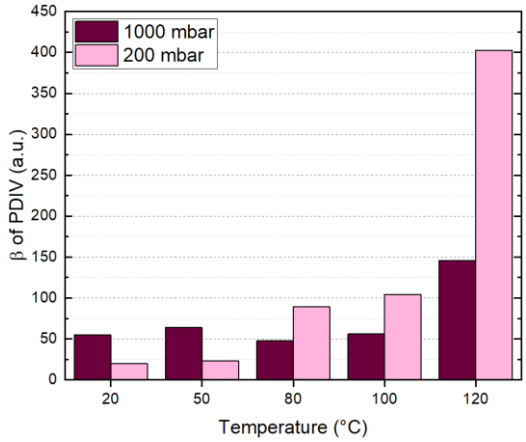

Fig. 7. Dispersion level of measured PDIV at 1000 and 200 mbar as a function of T.

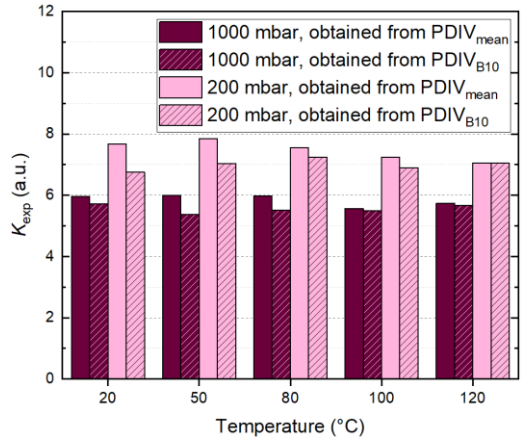

Fig 8. K at 1000 and 200 mbar as a function of T obtained from $\mathrm{PDIV}_{\mathrm{mean}}$ and $\mathrm{PDIV}_{\mathrm{B10}}$.

B. Schumann Constant (K)

Fig. 8 illustrates the calculated values of K based on the measured mean and B10 of the PDIV peak at GL and CA vs T. It shows that K remains nearly stable vs T variations at one specified p (i.e., 1000 mbar and 200 mbar) which is an important finding for PDIV modelling. This stability is more evident if it refers to $\mathrm{PDIV}_{\mathrm{B10}}$ which can be attributed to (12) and $A_{\mathrm{B10}} < A_{\mathrm{mean}}$, where B10 of PDIV shows a lower change against T. The average value of K at 1000 mbar from 20°C to 120°C is 5.84 and 5.56 based on $\mathrm{PDIV}_{\mathrm{mean}}$ and PDIVB_{10},

respectively. K is larger at CA than GL, and its mean value in the T range equals 7.47 and 7 acquired from $PDIV_{mean}$ and $PDIV_{B10}$, respectively. Considering the highest T (i.e., 120°C), since β of PDIV is the highest (i.e., dispersion is the lowest), referring to the mean value of PDIV or B10 of PDIV results in almost the same K at a specified p.

Fig. 9 demonstrates that the ratio of attained K at 200 mbar to 1000 mbar against T remains almost constant based on the mean and B10 of PDIV. Thus, the impact of p on K predominates over the effect of T variations. The average value of this ratio from 20°C to 120°C equals 1.28 and 1.26 obtained from $PDIV_{mean}$ and $PDIV_{B10}$, respectively.

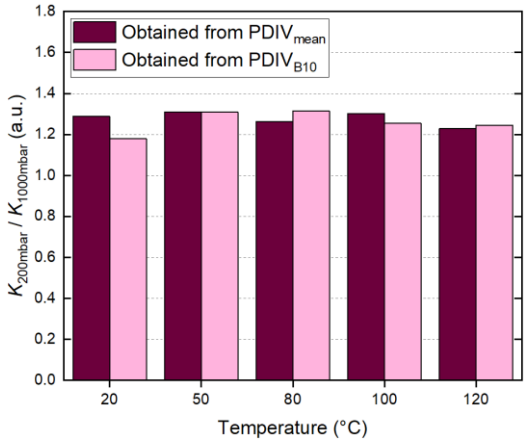

Fig 9. The ratio of K at CA to GL as a function of T obtained from $PDIV_{mean}$ and $PDIV_{B10}$.

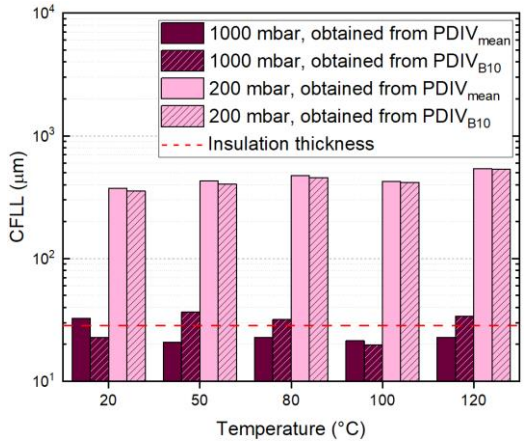

Fig. 10. CFLL at 1000 and 200 mbar as a function of T obtained from $PDIV_{mean}$ and $PDIV_{B10}$. (The dashed red lines show the wire insulation thickness)

C. CFLL

Fig. 10 shows the behaviour of CFLL across which the earliest discharge event takes place as a function of T. It is worthwhile to highlight that the CFL is always found in the critical region of α_{eff} curves (Fig. 2). Therefore, that zone has a decisive role in determining CFLL. Fig. 10 displays that CFLL is significantly longer at CA compared with GL. In other words, the electric field is more concentrated in the air rather than the solid insulation, implying a lower voltage drop across the wire insulation thickness at CA [6]. The larger CFLL can be ascribed to the movement of the critical region of α_{eff} towards lower electric fields at CA, thus longer FLLs (Fig. 2). A longer CFLL provides a further distance for an electron to accelerate across the FL. Thus, it gains sufficient kinetic energy to ionize other molecules on its path, reaching the critical number of electrons in the head of the avalanche at a lower applied voltage, leading to a lower PDIV at CA. In addition, it can be understood that the impact of reduced p on the increase of CFLL is much stronger than the influence of higher T although there is a gas density reduction in both cases. Indeed, the T rise effect on CFLL extension is more obvious at 200 mbar where it gets longer at 120°C than 20°C about 1.44 and 1.51 times based on $PDIV_{mean}$ and $PDIV_{B10}$, respectively. However, this effect is less tangible at 1000 mbar especially if it refers to $PDIV_{mean}$ where CFLL stays almost stable around 21.97 µm well below the insulation thickness at higher T values than 20°C.

Although CFLL is considered only inside the air based on SCSIC, the insulation thickness shown in Fig. 10 can suggest a critical cavity diameter for the wire insulation. Interestingly, this alludes that even in the presence of a cavity as large as the insulation thickness, the discharge events occur more likely in the surrounding air rather than inside the void itself at CA, regardless of the T value. However, at least one of the CFLLs attained from $PDIV_{mean}$, or $PDIV_{B10}$, is shorter than insulation thickness at different T values at GL, especially at 100°C, where both obtained values for CFLL remain lower than insulation thickness.

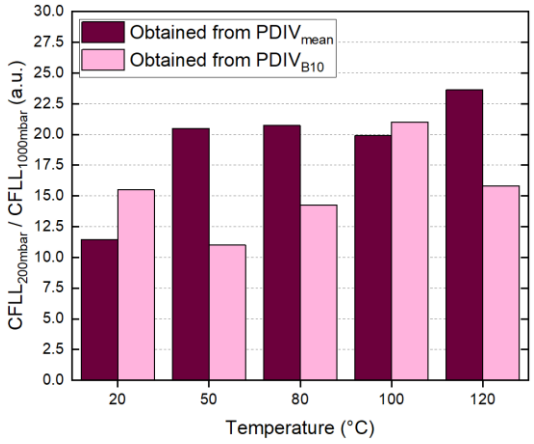

Fig 11. The ratio of CFLL at CA to GL as a function of T obtained from $PDIV_{mean}$ and $PDIV_{B10}$.

Fig. 11 indicates that the maximum and minimum ratio of CFLL at CA to GL vs T are acquired at 120°C and 20°C, respectively, based on $PDIV_{mean}$, where it varies from 23.6 to 11.6 times from the highest T (120°C) to the lowest T (20°C). Therefore, both reduced p and T rise make the CFLL longer since both result in a lower gas density. However, referring to B10 of PDIV delivers the maximum and minimum of this ratio at 100°C and 50°C, respectively, fluctuating between 21 and 11 times in the considered T range.

D. Effective Ionization Coefficient of Air

Fig. 12 shows the variations of effective ionization of air

(α_{eff}) corresponding to the CFL at GL and CA vs *T*.

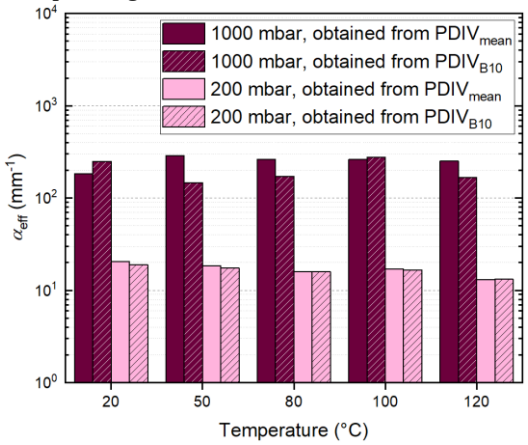

Fig. 12. α_{eff} at 1000 and 200 mbar as a function of *T* obtained from PDIV$_{mean}$ and PDIV$_{B10}$.

It illustrates that α_{eff} is remarkably weaker at CA than GL for different *T* values. Indeed, a lower α_{eff} at reduced *p* relevant to CA leads to an electron needs to move across a longer FL to reach the critical number of electrons in the head of the avalanche to initiate a discharge event, resulting in a longer CFL at CA (Fig. 10). Fig. 12 demonstrates that α_{eff} reduces vs *T* rise at 200 mbar which is an opposite trend compared to CFLL trend (Fig. 10). Considering 200 mbar, the ratio of α_{eff} at 120°C to that of 20°C is about 0.64 and 0.69 times based on PDIV$_{mean}$ and PDIV$_{B10}$, respectively. Regarding 1000 mbar and based on PDIV$_{mean}$, α_{eff} remains almost steady around 265.2 mm^{-1} from 50°C to 120°C, while its weakest value observed at the lowest *T* (i.e., 20°C) equals 182.3 mm^{-1}.

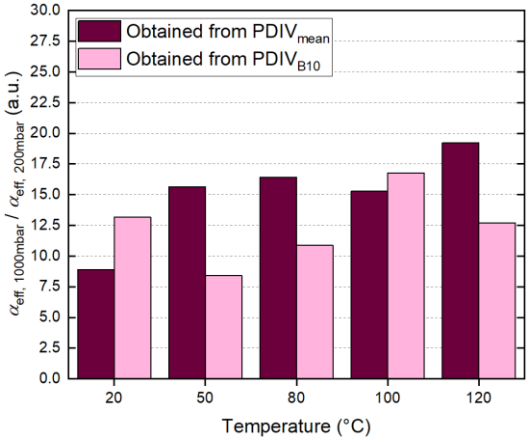

Fig 13. The ratio of α_{eff} at GL to CA as a function of *T* obtained from PDIV$_{mean}$ and PDIV$_{B10}$.

Fig. 13 illustrates that the maximum and minimum ratio of α_{eff} at GL to CA vs *T* are obtained at 120°C and 20°C, respectively, based on PDIV$_{mean}$, where it changes from 19.22 to 8.88 times from the highest *T* (120°C) to the lowest *T* (20°C). However, referring to B10 of PDIV delivers the maximum and minimum of this ratio at 100°C and 50°C, respectively, varying between 16.77 and 8.4 times in the considered *T* range.

Figs. 11 and 13 reveal a direct relationship between the ratio of CFLL at CA to that of GL and the proportion of α_{eff} at GL to that of CA. For example, both have minimum and maximum at the same *T* for the particular streamer inception probability that is being calculated.

E. Discharge Electric Field

Fig. 14 depicts the changes in the electric field along the CFL known as the streamer inception electric field (E_{inc}) at GL and CA as a function of *T*.

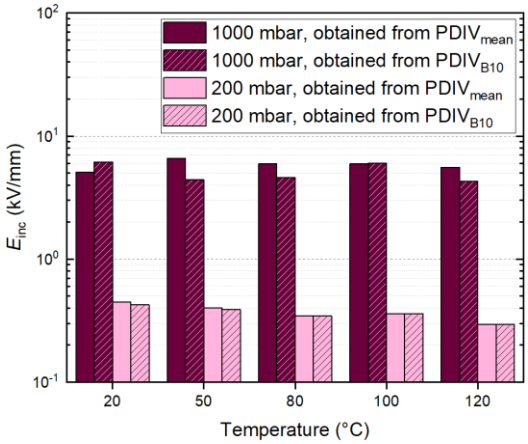

Fig. 14. E_{inc} at 1000 and 200 mbar as a function of *T* obtained from PDIV$_{mean}$ and PDIV$_{B10}$.

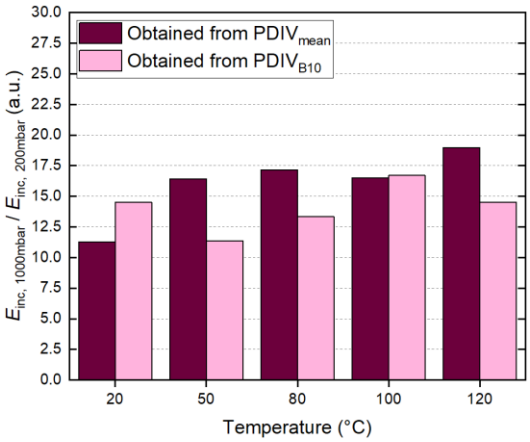

Fig 15. The ratio of E_{inc} at GL to CA as a function of *T* obtained from PDIV$_{mean}$ and PDIV$_{B10}$.

Figs. 14 and 12 demonstrate that the trends of E_{inc} and α_{eff} are the same vs *T*. Therefore, like α_{eff}, E_{inc} is considerably lower at CA than GL from 20°C to 120°C. Indeed, at CA, α_{eff} and CFL are weaker and longer, respectively, than GL. However, the latter impact prevails at CA, providing more acceleration, thus more kinetic energy, for a single initial electron to ionize the air molecules across its discharge path. Hence, reaching the critical number of electrons in the head of the avalanche at CA is realized across a longer CFL (Fig. 10) characterized by a lower electric field (Fig. 14). Fig. 14 reveals that E_{inc} decreases as a function of *T* rise at 200 mbar which is a similar and opposite trend compared to α_{eff} (Fig. 12) and CFLL (Fig. 10) trends, respectively. Interestingly like α_{eff}, the ratio of E_{inc} at 120°C to that of 20°C is about 0.65 and 0.69

times referring to $PDIV_{mean}$ and $PDIV_{B10}$, respectively, at CA (200 mbar). Considering 1000 mbar and based on $PDIV_{mean}$, E_{inc} stays almost stable at about 6 kV/mm from 50°C to 120°C, while its smallest value corresponds to the lowest T (i.e., 20°C) equals 5 kV/mm.

Interestingly, Figs. 15, 13, and 11 substantiate that the ratio of E_{inc} at 1000 mbar to 200 mbar (Fig. 15), the α_{eff} ratio at the same p levels as E_{inc} (Fig. 13), and the CFLL ratio at the reversed p levels (i.e., 200 mbar to 1000 mbar) (Fig. 11) follow the same pattern as a function of T. For instance, all three mentioned ratios reach their minimum and maximum values at the same T for the specific streamer inception probability referred to in the calculations.

Fig. 15 represents that the maximum and minimum ratio of E_{inc} at 1000 mbar to 200 mbar vs T occur at 120°C and 20°C, respectively, acquired from $PDIV_{mean}$, where it fluctuates from 18.98 to 11.28 times from 120°C to 20°C. However, referring to B10 of PDIV gives the maximum and minimum of this ratio at 100°C and 50°C, respectively, varying between 16.69 and 11.37 times.

V. PDIV Modelling Based on SCSIC

The disadvantage of the introduced simple linear regression model (12) for PDIV vs T is that it is only valid for the specific wire under investigation (i.e., specified insulation thickness and permittivity). Therefore, (12) is not reliable for a wire with a different insulation grade (i.e., insulation thickness) or various insulation types (i.e., permittivity). Indeed, (12) should be re-tuned based on the findings of a new experimental test campaign performed on the wire featuring different permittivity and/or thickness. In other words, the applicability/validity of (12) is limited at the tested wire. Relying on SCSIC, the developed PD model reveals superiority comprehensiveness because it accounts for the electric field distribution and the surrounding air-swarming parameters at several combinations of T and p.

In the following, the involving steps and iterations used to estimate PDIV [11] based on SCSIC as a function of T at GL (1000 mbar) and CA (200 mbar) are described:

1) Set K to the obtained value experimentally at GL and CA considering the desired PDIV percentile or streamer inception probability as summarized in Table II.

TABLE II
THE MEAN VALUE OF OBTAINED K FROM 20°C TO 120°C AT GL AND CA BASED ON $PDIV_{MEAN}$ AND $PDIV_{B10}$

pressure & percentile	1000 mbar-mean	1000 mbar-B10	200 mbar-mean	200 mbar-B10
K	5.845	5.556	7.472	6.994

2) Import the FLLs and their corresponding electric field intensity in the air wedge between the two wires simulated by COMSOL for a unit voltage (Fig. 1). Initialization of PDIV by e.g., 100 V and use (10) to update the electric field magnitude along each FL.

3) Import α_{eff} as a function of the electric field computed by BOLSIG+. Start from the shortest to the longest FLs, evaluate $K \leq \int_0^{x_c} \alpha_{eff}(x) \cdot dx$ for all the FL numbers, n_{FL}. Once it is fulfilled, stop the iteration, and report the applied voltage as PDIV, otherwise go back to step 2), increasing the applied voltage by e.g., 1 V. For the sake of clarity, Fig. 16 summarizes the above-mentioned steps in the iterative approach to model PDIV [21].

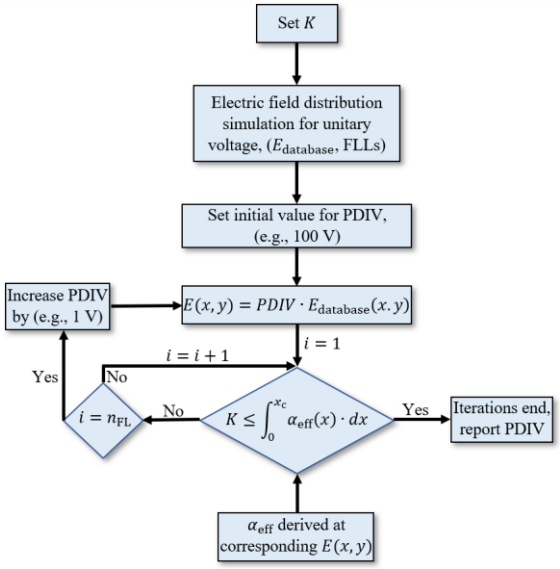

Fig. 16. A flowchart to visualize the steps involved in the iterative approach to estimate PDIV.

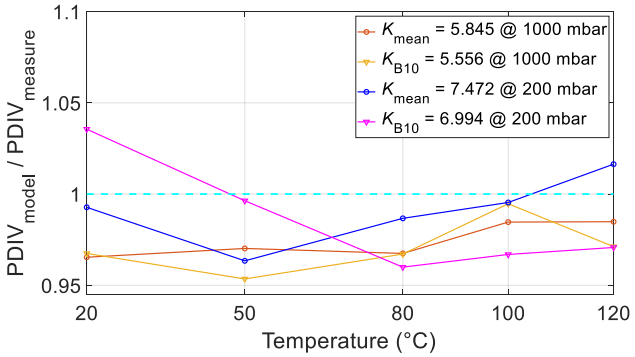

Fig. 17. The ratio of modelled and measured PDIV as a function of T.

Fig. 17 illustrates the ratio of modelled PDIV, using the four K values listed in Table II. Overall, it demonstrates that predicted PDIVs at CA and GL based on all the K values are reasonable, with an accuracy of more than 95%. The results are conservative except for two slight overestimations for 200 mbar at 20°C (3.56%) and 120°C (1.64%) using K_{B10} and K_{mean}, respectively. The comparison of modelled PDIV based on K_{mean} and K_{B10} reveals that the former delivers more accurate predictions. Indeed, K_{B10} is only precise at 100°C and 50°C for GL and CA, respectively. A lower determination coefficient (R^2) of $PDIV_{B10}$ fitted to the linear regression (12) (i.e., R^2 = 0.76) at CA can explain a lower accuracy of PDIV prediction using K_{B10} at 200 mbar based on SCSIC.

The proposed PDIV modelling approach could be applicable also to motor temperatures lower than 20°C (i.e., a lower limit of the investigated temperature range), although

such an operating temperature is very unlikely to occur in actual conditions due to the heat generated by the Joule effect within the motor windings. The validity of the PDIV model can be maintained at temperatures below 20°C by adjusting the inputs for calculating using BOLSIG+ and by measuring and considering the relative permittivity at lower temperatures for electrostatic calculations. The only potential limitation could be the need to conduct PDIV tests at these lower temperatures, which are necessary for deriving *K*.

VI. Conclusion

This contribution clarifies that the PDIV ratio at CA to GL is almost stable, independent of *T*, in the 20°C–120°C range. In addition, the PDIV dispersion level at CA decreases as *T* increases. Regarding the SIPs, the acquired *K* from B10 of the PDIV remains nearly constant vs *T* variations for a specified *p*. However, it is higher at CA than GL by about 1.3 times, regardless of *T*, manifesting a larger avalanche size at CA under PDIV. It is clarified that α_{eff} and E_{inc} are weaker at CA, decreasing with *T* rise, while the opposite stands for CFLL, where it is significantly larger at CA, enlarging with *T* enhancement. Although both *p* drop and *T* ascend lead to the gas number density reduction, the results reveal that the impact of *p* decrement on CFLL and its correspondents α_{eff} and E_{inc} from GL to CA is more considerable than the effect of *T* increment from 20°C to 120°C. The PDIV model predicts PDIV with more than a 95% degree of accuracy. It is demonstrated that PDIV modelling as a function of *T* based on the *K* value obtained from $PDIV_{mean}$ is more accurate than the acquired value from $PDIV_{B10}$, in particular at CA. The proposed PDIV model can help electric machine designers achieve a more reliable design for the winding turn-turn insulation of inverter-fed motors for aerospace applications. In fact, the key advantage of having a quick and precise model that can predict PDIV is the ability to make design decisions without having to run the entire experimental campaign if the tested wire is used for the machine winding.

References

[1] C. Li, Y. Yang, G. Xu, Y. Zhou, M. Jia, S. Zhong, Y. Gao, C. Park, Q. Liu, Y. Wang, and S. Akram, "Insulating materials for realising carbon neutrality: Opportunities, remaining issues and challenges," *High Voltage*, vol. 7, no. 4, pp. 610-632, 2022.

[2] G. Buticchi, P. Wheeler and D. Boroyevich, "The more-electric aircraft and beyond," *Proceedings of the IEEE*, vol. 111, no. 4, pp. 356-370, April 2023.

[3] Cavallini, D. Fabiani and G. C. Montanari, "Power electronics and electrical insulation systems - Part 1: Phenomenology overview," *IEEE Electr. Insul. Mag.*, vol. 26, no. 3, pp. 7-15, May-June 2010.

[4] V. Madonna, P. Giangrande, W. Zhao, H. Zhang, C. Gerada and M. Galea, "Electrical machines for the more electric aircraft: partial discharges investigation," *IEEE Trans. on Ind. Appl.*, vol. 57, no. 2, pp. 1389-1398, March-April 2021.

[5] L. Lusuardi, A. Rumi, A. Cavallini, D. Barater and S. Nuzzo, "Partial discharge phenomena in electrical machines for the more electrical aircraft. part II: impact of reduced pressures and wide bandgap devices," *IEEE Access*, vol. 9, pp. 27485-27495, 2021.

[6] A. Rumi, L. Lusuardi, A. Cavallini, M. Pastura, D. Barater and S. Nuzzo, "Partial discharges in electrical machines for the more electrical aircraft. part III: preventing partial discharges," *IEEE Access*, vol. 9, pp. 30113-30123, 2021.

[7] A. Cavallini, D. Fabiani and G. C. Montanari, "Power electronics and electrical insulation systems - part 2: life modeling for insulation design," *IEEE Electr. Insul. Mag.*, vol. 26, no. 4, pp. 33-39, July-Aug. 2010.

[8] A. Rumi, J. G. Marinelli, D. Barater, A. Cavallini and P. Seri, "The challenges of reliable dielectrics in modern aerospace applications: the hazard of corona resistant materials," *IEEE Trans. Transp. Electrification*, vol. 8, no. 4, pp. 4646-4653, Dec. 2022.

[9] A. Rumi, J. G. Marinelli, P. Seri, M. Kohler and A. Cavallini, "Performance of corona resistant insulation for aerospace," in *2021 IEEE EIC*, Denver, CO, USA, 2021, pp. 22-25.

[10] A. Rumi, J. G. Marinelli, A. Cavallini and P. Seri, "Can corona resistant wires ensure reliability in aerospace machine insulation?," in *2022 IEEE EIC*, Knoxville, TN, USA, 2022, pp. 309-312.

[11] L. Lusuardi, A. Cavallini, M. G. de la Calle, J. M. Martínez-Tarifa and G. Robles, "Insulation design of low voltage electrical motors fed by PWM inverters," *IEEE Electr. Insul. Mag.*, vol. 35, no. 3, pp. 7-15, May-June 2019.

[12] N. H. Malik, "Streamer breakdown criterion for compressed gases," *IEEE Trans. Electr. Insul.*, vol. EI-16, no. 5, pp. 463-467, Oct. 1981.

[13] W. O. Schumann, "Über das minimum der durchbruchfeldstärke bei kugelelektroden," *Arch. Elektrotech. (Berl.)*, vol. 12, pp. 593-608, 1923.

[14] L. Lusuardi, "Towards a partial discharge free insulation system for the more electrical transportation," Ph.D. dissertation, Dept. of Ing. Energ. Elettr. e Inf. "Guglielmo Marconi", Univ. of Bologna, Bologna, Italy, March 2020.

[15] H. Naderiallaf, P. Giangrande and M. Galea, "Experimental considerations on the possible impact of space charge accumulation on partial discharges activity for wire insulations," in *2022 IEEE ICD*, Palermo, Italy, 2022, pp. 82-85.

[16] H. Naderiallaf, P. Giangrande and M. Galea, "Characterization of PDIV, PDEV, and RPDIV in insulated wires under unipolar repetitive square wave excitations for inverter-fed motors," *IEEE Access*, vol. 11, pp. 51047-51063, 2023.

[17] H. Naderiallaf, P. Giangrande and M. Galea, "Experimental comparative investigation on alternative and commercially available wire insulations based on partial discharges activity," in *2023 INSUCON*, Birmingham, United Kingdom, 2023, pp. 107-111.

[18] H. Naderiallaf, P. Giangrande and M. Galea, "Investigating the effect of space charge accumulation on partial discharge activity for new and thermally aged glass fibre insulated wire," in *2023 INSUCON*, Birmingham, United Kingdom, 2023, pp. 39-43.

[19] G. J. M. Hagelaar and L. C. Pitchford, "Solving the Boltzmann equation to obtain electron transport coefficients and rate coefficients for fluid models," *Plasma Sources Sci. Technol.*, vol. 14, no. 4, pp. 722-733, 2005.

[20] "BOLSIG+ | Electron Boltzmann equation solver." [Online]. Available: http://www.bolsig.laplace.univ-tlse.fr/. [Accessed: Mar. 20, 2023].

[21] H. Naderiallaf, M. Degano, C. Gerada, "PDIV modelling for rectangular wire turn-to-turn insulation of inverter-fed motors through thermal ageing," *IEEE Trans. Electr. Insul.*, pp. 1-10, Aug. 2023.

[22] U.S. Committee on Extension to the Standard Atmosphere, "US Standard Atmosphere," National Oceanic and Atmospheric Administration, 1976.

[23] R. M. Goody and Y. L. Yung, *Atmospheric Radiation: Theoretical Basis*. Oxford University Press, 1995, pp. 1–15.

[24] *Winding Wires - Test Methods - Part 5: Electrical Properties*, IEC Std. 60851-5, 2008.

[25] M. Goldman, A. Goldman, and J. Gatellet, "Physical and chemical aspects of partial discharges and their effects on materials," in *1993 International Conference on Partial Discharge*, 1993, pp. 11-14.

[26] *Rotating electrical machines - Part 18-41: Partial discharge free electrical insulation systems (Type I) used in rotating electrical machines fed from voltage converters - Qualification and quality control tests*, IEC Std. 60034-18-41, 2019.

[27] L. Niemeyer, "A generalized approach to partial discharge modeling," *IEEE Trans. Dielectr. Electr. Insul.*, vol. 2, no. 4, pp. 510–528, Aug. 1995.

[28] TORLON® polyamide-imide design guide. [Online]. Available: https://www.kmsbearings.com/pub/media/itemlister/docs/Torlon_Design_Guide.pdf

[29] A. Rumi, J. Marinelli, and A. Cavallini, “Dielectric characterization of impregnating varnishes for inverter-fed motors,” in *2022 IEEE ICD*, Palermo, Italy, 2022, pp. 389-392.
[30] P. Wang, H. Xu, J. Wang, W. Wang and A. Cavallini, “Effect of repetitive impulsive voltage duty cycle on partial discharge features and insulation endurance of enameled wires for inverter-fed low voltage machines,” *IEEE Trans. Dielectr. Electr. Insul.*, vol. 24, no. 4, pp. 2123-2131, 2017.